Perpendicular Block Copolymer Microdomains in High Aspect-Ratio Templates

Wubin Bai‡, Karim Gadelrab‡, Alfredo Alexander-Katz, Caroline Ross*

Department of Materials Science and Engineering, Massachusetts Institute of Technology, Cambridge MA 02139
‡Equal Contributions
*caross@mit.edu

Abstract

Perpendicular orientation of lamellar microdomains in a high interaction parameter block copolymer was obtained within high aspect ratio gratings functionalized with a preferential sidewall brush. The experiments used polystyrene-block-polydimethylsiloxane with molecular weight 43 kg/mol within trenches made using interference lithography. The perpendicular alignment was obtained for both thermal and solvent annealing, using three different solvent vapors, for a range of film thicknesses and trench widths. A Pt layer at the base of the trenches avoided the formation of a wetting layer, giving perpendicular orientation at the substrate surface. The results are interpreted using self-consistent field theory simulation and a Ginzburg-Landau analytic model to map the energies of lamellae of different orientations as a function of the grating aspect ratio and the surface energies of the sidewalls and top and bottom surfaces. The model results agree with the experiment and provide a set of guidelines for obtaining perpendicular microdomains within topographic features.

Keywords: *Block Copolymer, self-assembly, perpendicular orientation, graphoepitaxy, solvent annealing, thermal annealing*

TOC Graphic
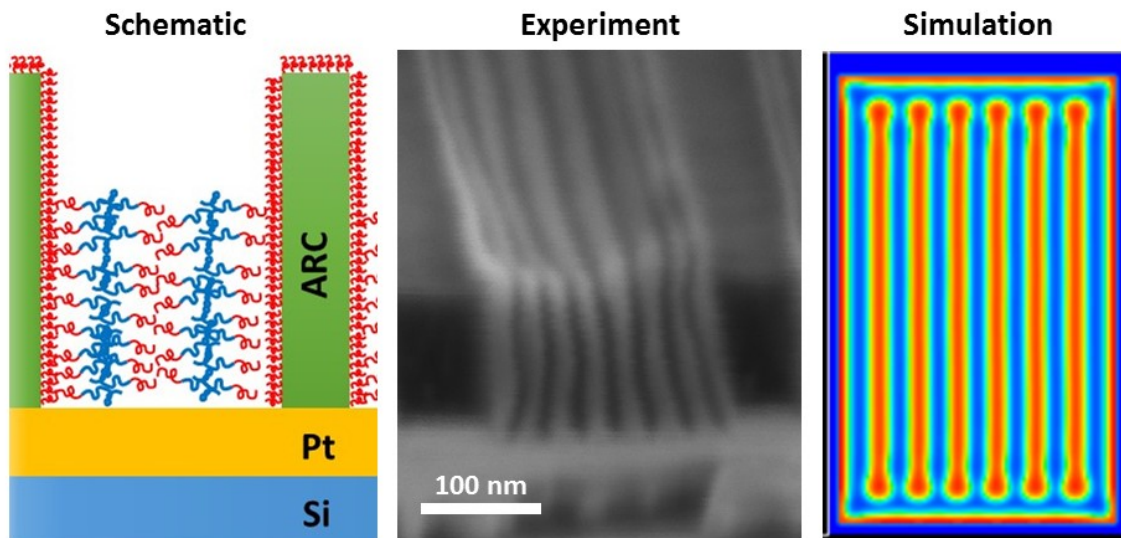
Article Text

Block copolymer (BCP) films have shown great utility in several technological applications including nanolithography for fabrication of integrated circuits,[1,2] magnetic storage media,[3,4] or sensors;[5–7] and in photonic crystals,[8–10] photovoltaics[11–13] and separation membranes,[14,15] as well as for making 3-dimensional nanostructures.[16] To obtain microphase separation at sub-10nm length scales, a high Flory-Huggins interaction parameter (χ) is desirable. However, high-χ BCPs usually exhibit large differences in surface affinity between the two blocks, leading to the formation of a surface layer of the lower surface energy block and favoring in-plane orientation of lamellae or cylindrical microdomains,[17] which is exacerbated if the substrate is also preferential to one block. This is undesirable in applications where through-thickness features are required, such as porous membranes or high-aspect-ratio structures for pattern transfer.

Perpendicular (vertical) orientation of block copolymer microdomains can be produced by several methods, including i) a neutral top coating and neutral substrate brush that minimize the interfacial energy difference between the blocks at the air and substrate interfaces respectively;[17–19] ii) a specifically designed molecular architecture[20–22] such as a brush or multi-arm BCP that can form microdomains oriented out-of-plane without modification of the underlying substrate, due to the entropic penalty associated with the packing of the side chains;[22] and iii) modifying the annealing process to use a solvent concentration gradient,[18,23] temperature gradient,[24,25] electric[26] or magnetic field[27], chemoepitaxy and/or graphoepitaxy,[28] and electrospray deposition[29] to induce out-of-plane alignment of self-assembled microdomains. These methods have been used successfully in various BCP systems, but become more challenging as the blocks become

more incompatible and the alignment method has to overcome a greater surface energy difference. In this article, perpendicular alignment of a high-χ lamellar BCP is demonstrated, not by minimizing the differences in surface energy of the blocks, but instead taking advantage of preferential wetting at the vertical sidewalls of high aspect-ratio templates. There have been examples of lamellar BCP microphase separation in high aspect ratio pores[30,31] but the effects of varying aspect ratio and surface chemistry have not been quantified.

A lamella-forming polystyrene-*block*-polydimethylsiloxane (PS-*b*-PDMS) with molecular weight M_w = 43 kg/mol, volume fraction f_{PDMS} = 49%, PDI = 1.08, designated SD43, was used to demonstrate orientation control in high aspect-ratio gratings. The room-temperature χ of PS-*b*-PDMS is reported as 0.14 - 0.27[31], and its high etch selectivity and the etch resistance of the PDMS makes it useful in nanolithography. After annealing, the PS block is removed by an oxygen plasma which oxidizes the PDMS, making a stable silica-rich nanostructure.

Laser interference lithography was used to fabricate the high aspect-ratio gratings. An interference pattern between two coherent laser beams (wavelength 350 nm) produced a grating pattern with period of ~200 nm and above in resist over a large substrate area without the use of a photomask.[34] The exposed and developed grating pattern was transferred from the photoresist into an underlying thick anti-reflective coating (ARC) layer, making trenches with width and depth $\geq$100 nm. To obtain a preferential surface, a PDMS brush polymer was grafted on the sidewalls and the trench floor. The surface affinity of the trench floor was modified by coating the substrate with electron-beam evaporated Pt prior to making the ARC grating. The brush layer did not graft well to the Pt, which does not bond to the hydroxyl group of the brush.[35] This led to a surface that was considerably less attractive to PDMS than the brush-coated sidewall was. A process flow showing the fabrication method is described in the supplementary material.

Interfacial interactions have a very important influence on the final equilibrium morphology of BCP self-assembly,[36,37] and form the basis of templating strategies.[16,38] In a high aspect-ratio template we consider three pairs of interfacial energies with respect to a lamellar-forming *A-B* diblock copolymer: γ_{Top}, γ_{Bot}, γ_{Side}, where γ is the interfacial energy and "Top", "Bot", and "Side" refer to the top (i.e. air surface), bottom and sidewall surface, respectively, as shown in figure 1a. The interfacial energy difference for each surface is defined as $\Delta\gamma = |\gamma_A - \gamma_B|$, i.e. a neutral surface has $\Delta\gamma = 0$ and a preferential surface has non-zero $\Delta\gamma$. The aspect ratio of the slab of BCP in the trench is defined as $R = t/w$ with t the thickness of the film and w the trench width. A perpendicular lamellar orientation is expected when the interaction energy with the sidewalls dominates, i.e. $\Delta\gamma_{Side}.t \gg \Delta\gamma_{Top}.w$, $\Delta\gamma_{Bot}.w$, i.e. $\Delta\gamma_{Side} \gg \Delta\gamma_{Top}/R$, $\Delta\gamma_{Bot}/R$. Therefore perpendicular self-assembled microdomains are promoted by large R and large $\Delta\gamma_{Side}$. In our experiment, we examine the effects of the surface energy of the grating walls (indicated in figure 1a) and the aspect ratio of the BCP in the trench. The fabricated trench depth was fixed at 450 nm, while the trench width varied from 150 nm to 500 nm, exemplified in Figs. 1b and S2b. To vary $\Delta\gamma_{Bot}$, a 20 nm thick platinum layer was inserted underneath the ARC, shown in Fig. 2. The surface tension of PS and PDMS on platinum has been reported as 33 mJ m^{-2}

and 25 mJ m^{-2} respectively.[39,40] Therefore the platinum surface has a slight preference to the PDMS block, but this is much smaller than the surface affinity of a PDMS-grafted surface.

We first describe the effect of aspect ratio R when the surface energy of the sidewall and bottom surfaces are equal. The ARC sidewalls and base of the trenches were made preferential to PDMS by grafting a hydroxy-terminated PDMS layer onto the template. The SD43 film thickness was varied from 100 nm to 550 nm. The samples of Figs. 1 and 2 were processed by solvent vapor annealing at room temperature,[41] and the depth of the trenches was 550 nm. Previous studies reported that the choice of solvent composition and partial pressure, the swelling rate and solvent removal rate affect the final morphology and the microdomain orientation.[42,43] We examined three different solvents: a selective solvent mixture (toluene: heptane vapor from a 3:1 volumetric ratio, in which heptane preferentially swells PDMS and toluene is weakly preferential), a selective solvent (cyclohexane) which preferentially swells PDMS, and a selective solvent (acetone) which preferentially swells PS (Table S1 in the supplementary material). For each solvent the final morphology depended primarily on the aspect ratio and surface chemistry, except that cyclohexane led to a morphological transition which will be described later (Fig. 1f).

In a trench width of 450 nm, a 100 nm thick BCP film formed in-plane (horizontal) lamellae (Fig. 1c1) in a toluene:heptane anneal. Perpendicular lamellae were observed in a 230 nm thick film (Fig. 2 and 1d). We believe that the perpendicular orientation in the 230 nm film, where the aspect ratio < 1, is aided by the swelling of the film and by solvent concentration gradients during the anneal. A 500 nm thick film in a 450 nm wide trench (Fig. S2d) formed lamellae with straighter interfaces and with a PDMS wetting layer at the bottom surface, due to the PDMS-brush. A 550 nm thick film in a 450 nm trench (Fig. 1e) in an acetone anneal produced highly oriented perpendicular lamellae parallel to the sidewalls. In general, acetone anneals produced more wetting and interconnections between lamellae at the base of the trench than toluene:heptane anneals. The top air/film interface always favored a PDMS wetting layer, due to its low surface energy,[41] but in these images this top in-plane layer was removed by the reactive ion etch and is usually not visible. Regions of an in-plane lamella at the top are visible in Fig. 1d and S2c.

In comparison, when the trench width was narrowed down to 170 nm and the sample was processed by cyclohexane solvent vapor annealing, the effective increase in PDMS volume fraction led to a transition to a perforated lamella structure standing perpendicular to the substrate, in which the PDMS lamellae are connected by bridges through the PS (Fig. 1f).

A high aspect ratio trench with PDMS-preferential sidewalls therefore favors perpendicular lamellae, except at the top and bottom surfaces. To avoid a wetting layer at the bottom surface, a thin layer of Pt was deposited on the substrate prior to forming the grating (Fig. 2a, schematic of sample; Fig. S2b, tilted SEM image). The PDMS brush is not expected to graft to the Pt surface, in contrast to its grafting to the ARC sidewall

during the brush treatment process, making the sidewall surface more preferential to the PDMS block than bottom surface. The importance of the topography and surface chemistry can be seen in a 2 μm-thick SD43 film shown in cross-section in figure 2b. Excellent perpendicular alignment of the lamellae was achieved within the trench, but above the patterned area the polymer self-assembled into its expected lamellar structure parallel to the substrate. The figure clearly shows the ability of the polymer to switch between two orthogonal orientations to satisfy the imposed boundary conditions, and shows that the perpendicular structure is not a metastable state due to directional evaporation of the solvent.

Fig. 2c shows a similar sample with 400 nm thick SD43 in which several layers of parallel lamellae are present at the air surface. Fig. 2d shows the same film in which the top parallel lamellae were removed by applying high power (450 W) CF_4 and O_2 plasma for 50 s, planarizing the structure down to $t_r = 150$ nm thickness, and demonstrating how smaller aspect ratio perpendicular lamellae can be produced. In Fig. 2b-d the lamellae form perpendicular to the Pt producing little or no PDMS wetting at the bottom. Fig. S2a and S2c show further examples of vertical lamellae in trenches with a Pt base. In Fig. S2a the vertical orientation was produced in a film 150 nm thick in 300 nm wide trenches. This sample was not processed with the high power etch to better preserve the top layer morphology, showing a tilting of the PDMS lamellae at the top surface to form the thin wetting layer.

Fig. 3 shows that thermal annealing can also produce perpendicular lamellae in high aspect-ratio gratings. Samples with a SD43 thickness of 445 nm (Fig. 3a) and 311 nm (Fig. 3b) in 350 nm deep, 200 nm wide gratings with a Pt base were annealed at 150 ^{o}C for 24 hr in vacuum. In Fig. 3a, lamellae within the gratings were aligned along the grating, but the film just above the grating showed a transition to in plane orientation. Thinner films (Fig. 3b) were well aligned through the thickness, after removing the PDMS layer at the air interface. Figs. 3c and 3d show thermal annealing for a 450 nm wide trench with both sidewall and bottom layer made of ARC. Perpendicular lamellae were found for SD43 thickness of 227 nm and 394 nm, but a thin PDMS wetting layer at the bottom connected the lamellae, due to the grafted PDMS brush at the base.

The ARC sidewalls in Figs. 3a,b,c showed a slight taper such that the trench width was smaller at the base than the top. This led to formation of an extra lamella in nearly all the trenches, i.e. one lamella branched into two, indicated in Fig. 3a.

To explain the experimental results, a self-consistent field theoretic (SCFT) simulation was employed to study the equilibrium morphology of a diblock copolymer inside a trench confinement as a function of aspect ratio and surface affinity. A detailed description of the simulation method is given in the supplementary material. Here we consider a 2D rectangular volume of width $L_x = 30R_g$ (where R_g is the radius of gyration) and a varying height L_z. This represents a cross-sectional view of the trench-confined BCP self-assembly. The geometry of the trench is varied to consider a range of aspect ratios $R \equiv L_z/L_x \in$ [0.8, 1.0, 1.2, 1.4, 1.6, 1.8]. The four boundaries of the computational cell are made attractive to block A. The top surface has an independent strength of

attraction w_{Top} to simulate the low surface energy of PDMS,[41] while the three remaining surfaces have equal affinity w_{Surr} to A simulating a brush layer coating on the trench sidewalls and substrate. Hence, by modulating the strength of attraction in the model, we modify the interfacial interactions at the boundaries. The volume fraction f of the block copolymer is set to 0.5, and the degree of incompatibility (= χN, where N is degree of polymerization) to 14 in order to represent the lamella-forming PS-PDMS block. In this 2D simulation, the effect of aspect ratio, free top surface affinity, and surrounding walls affinities on the alignment of the lamellar structure are investigated.

To compare the relative stabilities of perpendicular and in plane orientations, the analysis is first performed by seeding a vertical or a horizontal self-assembled lamellar structure to the SCFT simulation. The structure is allowed to relax by evolving the fields at varying surface attraction strengths, w_{Top} and w_{Surr}. This led to parallel lamellae with a PDMS wetting layer at each surface. The free energies of both vertical F_V and horizontal F_H aligned lamellar structures are calculated following eq. S1. Figure 4 shows the corresponding free energy difference F_V-F_H calculated for R values 0.8, 1.0 and 1.2 (the free energy difference for larger R values is shown in Fig. S3). For R less than unity ($R = 0.8$) the free energy surface is predominantly positive. The horizontal lamellar structure is stable (white markers) when the surface attraction field is small and positive, $w_{Top} \geq 2$. Vertical lamellae (black markers) can be attained with small w_{Top} and wall attraction $w_{Surr} > w_{Top}$. Increasing both w_{Top} and w_{Surr} favors the horizontal lamellae. The behavior is switched when $R \geq 1$; the free energy difference is predominantly negative. The vertical structure becomes stable for smaller w_{Surr} while larger w_{Top} is needed to realize a horizontal structure. The vertical structure is favored when increasing both w_{Top} and w_{Surr}. Increasing R raises the free energy difference between both morphologies, giving more stability to the vertical morphology.

While the free energy analysis aligns with the experimental work, there are regions in the parameter space where the free energy differences are quite small in magnitude, ~ 0.01 nVk_bT where V is the volume of the block copolymer and n the number of molecules per unit volume. These regions are primarily when w_{Top} and w_{Surr} are comparable and R is closer to unity. These almost degenerate situations would produce structures having mixed morphologies. It is insightful to observe the resulting polymer structure under these conditions.

To allow for the formation of kinetically trapped morphologies, SCFT simulations were also conducted under the surface conditions previously investigated in Fig. 4, but instead, the structure was self consistently evolved from random fields, simulating polymer phase separation from the disordered state. The final structures obtained from the simulation can be divided into three main categories: Horizontal lamellae, Mixed lamellae, and Vertical lamellae (representative results for $R = 1.4$ are shown in Fig. 5b). A 4D plot summarizes the results of the SCFT simulations in Fig. 5a. The scale of the x and y axes are the surface field strengths for the walls w_{Surr} and top surface w_{Top}, respectively. For each pair of (w_{Surr}, w_{Top}), a set of six color bars represents results for the six values of R. The color indicates Horizontal (white), Mixed (gray), or Vertical (black) lamellar orientations. To objectively classify each structure, a vertical and a horizontal defect-free

structure were employed as references for every R, and the characteristics of the self-assembly are then calculated using a correlation function between the reference and the model result. A polymer structure is considered vertical or horizontal when it has a correlation function higher than 0.7 with the corresponding reference structure (the density profiles of the SCFT simulations are provided in the supplementary information). The final structures agree very well with the free energy map in Fig. 4, except for the presence of mixed orientations which were not considered in Fig. 4 and which, once formed, could not anneal into parallel lamellae. However, the majority of the high-R simulations reached a defect-free equilibrium structure consisting of parallel lamellae with PDMS at each surface, and the overall order is improved by increasing the boundary attraction.

Mixed morphology (blue rectangles) prevails at low trench wall attraction w_{Surr} particularly at $R \sim 1$. The defect patterns demonstrate right angle bends mimicking the confining walls. The right angle bends create interlocked structures that are difficult to anneal. Additional structural characteristics are noticed in SCFT density maps. At low surface attraction strength, periodic short microdomains protrude from the surface towards the bulk of the polymer. These short microdomains become the seeds of a structure that is perpendicular to the surface. The short microdomains can merge to form arches at corners and even on the same surface, generating nonequilibrium defects. On the other hand, increasing surface attraction strength suppresses the extent of short microdomains and creates a uniform wetting layer on the surface. A propagating front from the surface then generates a structure parallel to it. For a defect-free structure surrounded by strong fields on all surfaces, the structure becomes disconnected from the surrounding surfaces as a flat wetting layer encapsulates the polymer domains. A circular cap is observed at both ends of every lamella (Figure S3).

The formation of mixed orientation lamellae was also observed experimentally. For example, a concentric structure of rectangular tubes was observed after prolonged annealing (24 hr, fig. 6a,b) while with the same toluene/heptane solvent anneal condition, a 3-hr anneal resulted in perpendicular lamellae (Fig. 1d). This sample had a final thickness of 240 nm, but based on the swelling ratio, this corresponded to a thickness of 400 nm during annealing, similar to the trench width. The transformation of parallel to concentric lamellae is interpreted as a change in the wetting conditions of the confining surfaces, and we employ SCFT to understand the conditions under which such a structure might emerge. A concentric tubular structure was seeded to a SCFT simulation and allowed to evolve under varying surface conditions (see Fig. 6b). The free energy of the structure is compared to a fully vertical or a fully horizontal morphology for a given trench aspect ratio $R = [0.8, 1.0, 1.2]$ and surface conditions. In plane lamellae are stable for $R = 0.8$, whereas vertical lamellae are stable for $R = 1.2$ (Fig. S4). While the free energy difference decreases as the surface fields are increased, the horizontal and vertical structures remain stable even when surface fields are doubled. The case of $R = 1$ on the other hand is particularly interesting. The vertical lamellae remain favorable at high surface fields but the free energy difference between the concentric structure and vertical one practically vanishes at $w_{Top} = 20$ and $w_{Surr} = 19$ reaching a value of $\sim 10^{-3} n V k_b T$. The asymptotic behavior of the plot asserts that the concentric structure can only be stable at

very high fields, compared to the vertical morphology. This means that for $R = 1$, low surface fields would result in a stable vertical structure that would become degenerate with a concentric structure when surface fields grow in magnitude. This would explain the experimental observation where the slow evaporation of solvent over the 24 hr anneal amplifies the surface fields confining the polymer and generates the concentric structure. In contrast, the shorter anneals are terminated by a rapid deswelling in air which preserves the morphology developed in the swelled state as it collapses in the out-of-plane direction.[44]

While SCFT provides an accurate description of the morphology of the confined block copolymers in specific cases, we employ a Ginzburg-Landau free energy expansion to provide analytical predictions of the effects of surface affinity and aspect ratio.[45] The analysis presented is an extension to the work of Tsori and Andelman.[46] The free energy of the system contains a bulk and a surface term, and is expanded in terms of an order parameter describing the deviation of the density of one of the blocks from its mean value. The surface free energy expression has a surface field contribution σ that describes the affinity of the surface to a particular block. In addition, an effective segregation contribution τ_s is employed to describe the deviation of χ from its bulk value at the surface. For a positive τ_s, order takes place at surfaces at a higher χ than the bulk.[47] The details of the formalism are described in the supplementary information. We first isolate the role of R by constructing a phase diagram for a system with identical surface conditions on all boundaries. Fig. 7a maps regions of stable horizontal lamellae (bright) and vertical lamellae (dark) for a system with a width of $2L_x = 4d_0$ and $\tau_s = 0.1hq_0^3$, where $q_0 \approx 1.95/R_g$, $d_0 = 2\pi/q_0$, and $h = 3/2 \times \rho c^2 (R_g/q_0)^2$ with $\rho = 1/Nb^3$, $c \sim 1$, $b =$ statistical segment length and R_g the radius of gyration (the definition of the terms is provided in the supplementary materials). Horizontal lamellae are stable when $2L_z$ is commensurate with the equilibrium periodicity of the BCP. By doing so, a minimum strain energy of confinement is attained, and a dip in the free energy curve of the horizontal lamellae is observed (see inset of Fig. 7a). This is reflected in the periodic behavior of the bright regions in Fig. 7a. More importantly, it is seen that there is a direct correlation between surface field σ and R. Vertical lamellae are generally stable when both R and σ are either high or low. At very low σ, the structure orientation is dominated by τ_s. The effect of τ_s was previously discussed by Tsori, et al,[47] where a positive τ_s caused a significant improvement in stability of structure normal to confining walls even when the walls were weakly attractive to one of the blocks. This is typically unexpected from the theory of strong segregation where slight preferentiality to one of the blocks results in a structure parallel to the surface. Matsen referred to this as a negative line tension at the intersections between the A/B interfaces and surfaces.[48] Hence in our case, the system gives preference to structures *normal* to the largest confining surface due to the effect of τ_s. This is translated into lamellae in the out of plane direction at low R, which switches to the in plane direction as R increases. This behavior is overwritten when σ increases in magnitude, as the system promotes structures that are rather *parallel* to the largest confining surface. This is further confirmed in Fig. 7b where the transition between parallel and perpendicular structures is pushed to a higher surface attraction σ when $\tau_s = 0.2hq_0^3$. Furthermore, we fixed the attraction potential of the top surface $\sigma_{Top} = 0.6hq_0^3\phi_q$, while maintaining $\tau_s = 0.2hq_0^3$ for all surfaces, in order to represent the air/film interface.

Fig. 7c shows the resulting phase diagram of the system. It is clear that biasing the top surface to attract one of the blocks strongly favors the horizontal structure (bright regions). Stability of the horizontal structure extends throughout the entire range of surface attraction at low R, while it extends to large wall attraction σ at high R. Hence, perpendicular structures in systems with large preferentiality towards the surface at the air/polymer interface are challenging. Increasing R would not suppress the surface effects. Sidewall attraction in addition to the minimization of local deviation of polymer segregation will counterbalance the free surface effects and produce vertical structures.

To summarize, we have introduced a simple fabrication protocol to create vertically standing lamellar structure from high-χ BCPs within high aspect ratio trenches that guide the self-assembly. The trench aspect ratio R and the surface energy difference between the sidewalls and the top and bottom surfaces were found to determine the lamellar orientation. Through free energy analysis, SCFT simulations were employed to determine the morphological stability under varying confinements and surface attraction strengths. A horizontal lamellar structure prevails at low R even for a low top surface attraction strength, while vertical structures prevail when $R > 1$ for a small trench wall attraction. Ginzburg-Landau free energy analysis further demonstrates the importance of commensurability between film height and natural polymer periodicity. In addition, a concentric tubular structure was fabricated by allowing the lamellae to fuse at top and bottom surfaces. SCFT free energy analysis suggests that the change of surface affinity is responsible for such a structural evolution. The self-assembled perpendicular lamellae are expected to be useful for pattern transfer in nanolithography applications, and can also be functionalized by processes such as sequential filtration synthesis, nanoparticle incorporation, and salt complexation. The development of concentric tubes opens the door to fabricate 3D BCP nanostructures by design of substrate and annealing process.

Methods

High Aspect ratio Trench Fabrication
Anti-reflective coating (ARC) was first spin coated on a Si wafer and then baked on a hotplate at 175$^{\mathrm{o}}$C for 60 s to induce crosslinking. Then 20nm SiO_2 was deposited by electron beam evaporation. A 200 nm PFI 88 photoresist was spin coated on top of the SiO_2 layer and baked on a hotplate at 90$^{\mathrm{o}}$C for 60s. The sample was exposed by an interference pattern that was generated from 2-beam coherent laser for several minutes using a Lloyds Mirror system. A post-exposure development was used to produce the photoresist grating. Then CF_4 plasma etching transferred the photoresist pattern into the SiO_2 layer, and an O_2 plasma transferred the pattern into the ARC layer to make high aspect ratio trenches. A schematic is shown in figure S1.

Brush treatment and Block Copolymer solution preparation
The hydroxyl-terminated polydimethylsiloxane (0.8 kg mol^{-1}, PolymerSource, Inc) was dissolved 5 wt.% in toluene and then spin coated on high aspect ratio templates at a spin speed of 2000 rpm. Then the samples were baked in a vacuum oven for 16 hr at a pressure of 2600 Pa (20 Torr) and temperature of 170 $^{\mathrm{o}}$C. After baking, the samples were rinsed with toluene to remove unreacted brush and then dried using N_2 gas. 43 kg mol^{-1}

PS-*b*-PDMS (PolymerSource, Inc. $f_{PDMS} = 0.5$) as 5 wt.% in toluene solution was spin coated onto the brush-treated templates at spin speed 3500 rpm.

Solvent Vapor Annealing
Solvent vapor annealing has been described in previous work.[41,49] Briefly, liquid toluene-heptane mixture, or cyclohexane, or acetone of 3 ml was placed in a glass annealing chamber of volume ~ 70 cm^3 with a lid. The sample was placed on a small stage above the liquid. The generated solvent vapor was absorbed by the polymer film and the degree of swelling (measured by a Filmetrics reflectometer) was tuned by altering the leakage of solvent vapor from the chamber. For three hour anneals there was remaining liquid solvent in the chamber, and the sample was deswelled within a few seconds by removing the lid of the chamber. For 24 hr anneals the solvent had fully evaporated so the condition corresponds to a slow deswelling.

Thermal Annealing
Samples were placed into a vacuum oven and annealed in 20 Torr at 150°C for 16 hr.

Reactive Ion Etching
To reveal the self-assembled nanostructure, a two-step reactive ion etching was applied. First, a 30 CF_4 and O_2 plasma with power 450 W and pressure 15 mTorr was performed to planarize the polymer film for 30s. Then, an O_2 plasma with power 90 W and pressure 6 mTorr was performed to selectively remove the PS block and partially oxidize the PDMS block into robust SiO_x.

Helium Ion Microscope
Cross-section images were obtained by imaging in a Helium Ion Microscope, which is based on the interaction between a helium ion beam and the sample.

Associated Content

Supporting Information

The Supporting Information [Process flow, Solubility parameters, Electron micrographs of additional samples of self assembled block copolymers in trenches, Methods and Computational details] is available free of charge on the ACS Publications website at DOI:

Corresponding Author

Caroline Ross, caross@mit.edu

Notes

The authors declare no competing financial interest.

References:

(1)   Yi, H.; Bao, X.-Y.; Tiberio, R.; Wong, H.-S. P. *Nano Lett.* **2015**, *15* (2), 805–812.

(2)   Black, C. T.; Ruiz, R.; Breyta, G.; Cheng, J. Y.; Colburn, M. E.; Guarini, K. W.; Kim, H.-C.; Zhang, Y. *IBM J. Res. Dev.* **2007**, *51* (5), 605–633.

(3)   Xiao, S.; Yang, X.; Edwards, E. W.; La, Y.-H.; Nealey, P. F. *Nanotechnology* **2005**, *16*, S324–S329.

(4)   Lin, C.-H.; Polisetty, S.; O'Brien, L.; Baruth, A.; Hillmyer, M. A.; Leighton, C.; Gladfelter, W. L. *ACS Nano* **2015**, *9* (2), 1379–1387.

(5)   Jung, Y. S.; Jung, W.; Tuller, H. L.; Ross, C. A. *Nano Lett.* **2008**, *8* (11), 3776–3780.

(6)   Guenther, M.; Kuckling, D.; Corten, C.; Gerlach, G.; Sorber, J.; Suchaneck, G.; Arndt, K. *Sensors Actuators B Chem.* **2007**, *126* (1), 97–106.

(7)   Bearzotti, A.; Bertolo, J. M.; Innocenzi, P.; Falcaro, P.; Traversa, E. *J. Eur. Ceram. Soc.* **2004**, *24* (6), 1969–1972.

(8)   Kang, Y.; Walish, J. J.; Gorishnyy, T.; Thomas, E. L. *Nat. Mater.* **2007**, *6* (12), 957–960.

(9)   Urbas, A. M.; Maldovan, M.; DeRege, P.; Thomas, E. L. *Adv. Mater.* **2002**, *14* (24), 1850–1853.

(10)   Fink, Y.; Urbas, A. M.; Bawendi, M. G.; Joannopoulos, J. D.; Thomas, E. L. *J. Light. Technol.* **1999**, *17* (11), 1963–1969.

(11)   Zhang, Q.; Cirpan, A.; Russell, T. P.; Emrick, T. *Macromolecules* **2009**, *42* (4), 1079–1082.

(12)   Tao, Y.; McCulloch, B.; Kim, S.; Segalman, R. A. *Soft Matter* **2009**, *5* (21), 4219.

(13)   Crossland, E. J. W.; Nedelcu, M.; Ducati, C.; Ludwigs, S.; Hillmyer, M. A.; Steiner, U.; Snaith, H. J. *Nano Lett.* **2009**, *9* (8), 2813–2819.

(14)   Kurihara, M.; Kamachi, M.; Stille, J. K. *J. Polym. Sci. Polym. Chem. Ed.* **1973**, *11* (3), 587–610.

(15)   Metz, S. J.; Potreck, J.; Mulder, M. H. V.; Wessling, M. *Desalination* **2002**, *148* (1-3), 303–307.

(16)   Ross, C. A.; Berggren, K. K.; Cheng, J. Y.; Jung, Y. S.; Chang, J.-B. *Adv. Mater.* **2014**, *26* (25), 4386–4396.

(17)   Bates, C. M.; Seshimo, T.; Maher, M. J.; Durand, W. J.; Cushen, J. D.; Dean, L. M.; Blachut, G.; Ellison, C. J.; Willson, C. G. *Science (80-.)*. **2012**, *338*, 775–779.

(18)   Kim, E.; Kim, W.; Lee, K. H.; Ross, C. A.; Son, J. G. *Adv. Funct. Mater.* **2014**, 6981–6988.

(19)   Han, E.; Stuen, K. O.; Leolukman, M.; Liu, C.-C.; Nealey, P. F.; Gopalan, P. *Macromolecules* **2009**, *42* (13), 4896–4901.

(20)   Verduzco, R.; Li, X.; Pesek, S. L.; Stein, G. E. *Chem. Soc. Rev.* **2015**.

(21)   Fenyves, R.; Schmutz, M.; Horner, I. J.; Bright, F. V; Rzayev, J. *J. Am. Chem. Soc.* **2014**, *136* (21), 7762–7770.

(22)   Hong, S. W.; Gu, W.; Huh, J.; Sveinbjornsson, B. R.; Jeong, G.; Grubbs, R. H.; Russell, T. P. *ACS Nano* **2013**, *7* (11), 9684–9692.

(23)   Son, J. G.; Gotrik, K. W.; Ross, C. A. *ACS Macro Lett.* **2012**, *1* (11), 1279–1284.

(24)   Bodycomb, J.; Funaki, Y.; Kimishima, K.; Hashimoto, T. *Macromolecules* **1999**, *32* (6), 2075–2077.

(25)   Singh, G.; Yager, K. G.; Berry, B.; Kim, H.-C.; Karim, A. *ACS Nano* **2012**, *6* (11), 10335–10342.

(26)   Olszowka, V.; Hund, M.; Kuntermann, V.; Scherdel, S.; Tsarkova, L.; Böker, A. *ACS Nano* **2009**, *3* (5), 1091–1096.

(27)   Majewski, P. W.; Gopinadhan, M.; Osuji, C. O. *J. Polym. Sci. Part B Polym. Phys.* **2012**, *50* (1), 2–8.

(28) Park, S.-M.; Stoykovich, M. P.; Ruiz, R.; Zhang, Y.; Black, C. T.; Nealey, P. F. *Adv. Mater.* **2007**, *19* (4), 607–611.

(29) Hu, H.; Choo, Y.; Feng, X.; Osuji, C. O. *Macromol. Rapid Commun.* **2015**.

(30) Xiang, H.; Shin, K.; Kim, T.; Moon, S.; Mccarthy, T. J.; Russell, T. P. *J. Polym. Sci. Part B Polym. Phys.* **2005**, *43* (23), 3377–3383.

(31) Shin, K.; Xiang, H.; Moon, S. I.; Kim, T.; McCarthy, T. J.; Russell, T. P. *Science* **2004**, *306* (5693), 76.

(32) Nose, T. *Polymer (Guildf).* **1995**, *36* (11), 2243–2248.

(33) Kennemur, J. G.; Yao, L.; Bates, F. S.; Hillmyer, M. A. *Macromolecules* **2014**, *47* (4), 1411–1418.

(34) Mojarad, N.; Gobrecht, J.; Ekinci, Y. *Sci. Rep.* **2015**, *5*, 9235.

(35) Chibani, S.; Michel, C.; Delbecq, F.; Pinel, C.; Besson, M. *Catal. Sci. Technol.* **2013**, *3* (2), 339–350.

(36) Edwards, E. W.; Montague, M. F.; Solak, H. H.; Hawker, C. J.; Nealey, P. F. *Adv. Mater.* **2004**, *16* (15), 1315–1319.

(37) Xu, T.; Hawker, C. J.; Russell, T. P. *Macromolecules* **2005**, *38* (7), 2802–2805.

(38) Stoykovich, M. P.; Müller, M.; Kim, S. O.; Solak, H. H.; Edwards, E. W.; de Pablo, J. J.; Nealey, P. F. *Science (80-.).* **2005**, *308* (5727), 1442–1446.

(39) Chaudhury, M. K. *Mater. Sci. Eng. R Reports* **1996**, *16* (3), 97–159.

(40) Kobayashi, H.; Owen, M. J. *Die Makromol. Chemie* **1993**, *194* (6), 1785–1792.

(41) Bai, W.; Hannon, A. F.; Gotrik, K. W.; Choi, H. K.; Aissou, K.; Liontos, G.; Ntetsikas, K.; Alexander-Katz, A.; Avgeropoulos, A.; Ross, C. A. *Macromolecules* **2014**, *47* (17), 6000–6008.

(42) Paik, M. Y.; Bosworth, J. K.; Smilges, D.-M.; Schwartz, E. L.; Andre, X.; Ober, C. K. *Macromolecules* **2010**, *43* (9), 4253–4260.

(43) Di, Z.; Posselt, D.; Smilgies, D.-M.; Papadakis, C. M. *Macromolecules* **2010**, *43*, 418–427.

(44) Gu, X.; Gunkel, I.; Hexemer, A.; Gu, W.; Russell, T. P. *Adv. Mater.* **2014**, *26* (2), 273–281.

(45)   Cohen, S.; Andelman, D. *Macromolecules* **2014**, *47* (1), 460–469.

(46)   Tsori, Y.; Andelman, D. *Eur. Phys. J. E* **2001**, *5* (5), 605–614.

(47)   Tsori, Y.; Andelman, D. *J. Chem. Phys.* **2001**, *115* (4), 1970.

(48)   Matsen, M. W. *J. Chem. Phys.* **1997**, *106* (18), 7781.

(49)   Gotrik, K. W.; Hannon, A. F.; Son, J. G.; Keller, B.; Alexander-Katz, A.; Ross, C. A. *ACS Nano* **2012**, *6* (9), 8052–8059.
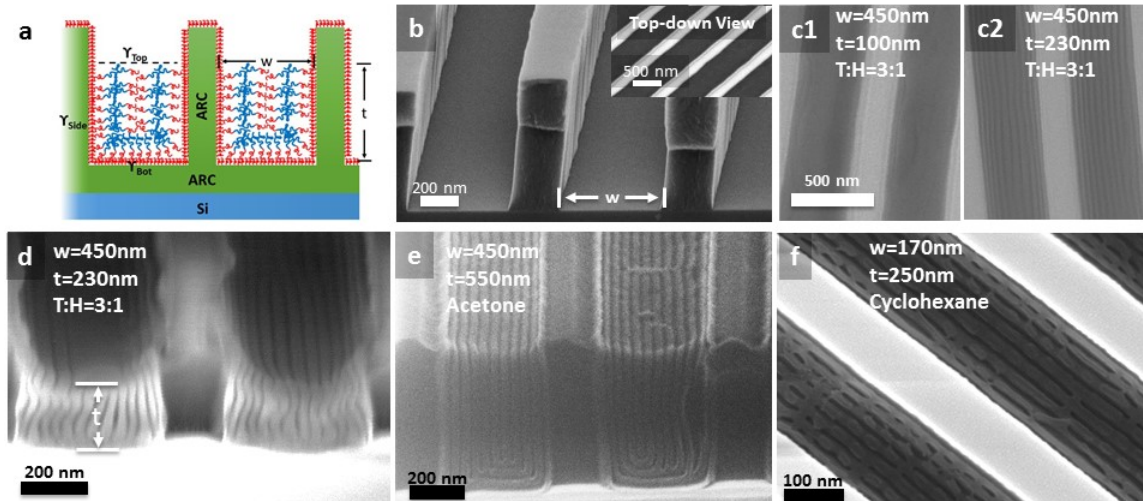
Figures

Figure 1. PDMS-brushed templates, solvent anneal. (a). A schematic of lamella-forming block copolymer film in a high aspect-ratio grating. γ_{Side}, γ_{Top}, γ_{Bot} are the interfacial energy at the sidewall, bottom and top surface. w is the width of the trench, t is the thickness of the film. Blue indicates the PDMS, red the PS blocks; (b). 75° SEM tilted view of a cross-section of a high-aspect ratio grating; inset shows top-down SEM of high-aspect ratio gratings; (c1). Top-down SEM view of a 100nm thick SD43 film showing in-plane lamellae after reactive ion etching (RIE). (c2). Top-down SEM view of a 230nm thick SD43 film showing out-of-plane lamellae after RIE; (d, e, f). Cross-section SEM of self-assembled perpendicular SD43 lamellae inside high aspect-ratio trench; 75° SEM tilted view. The lamella-forming SD43 PS-PDMS films were spin-cast with thickness (d) 230nm; (e) 550nm; (f) 250nm; (d), annealed under solvent vapor produced from toluene: heptane 3:1 volumetric mixture for 3 hr, showing a meniscus; (e), annealed under acetone solvent vapor for 3 hr. (f), annealed under cyclohexane solvent vapor for 3 hr; b-e, Trench width 450nm, depth 550nm. f, Trench width 170nm, depth 550nm. T: Toluene; H: Heptane.
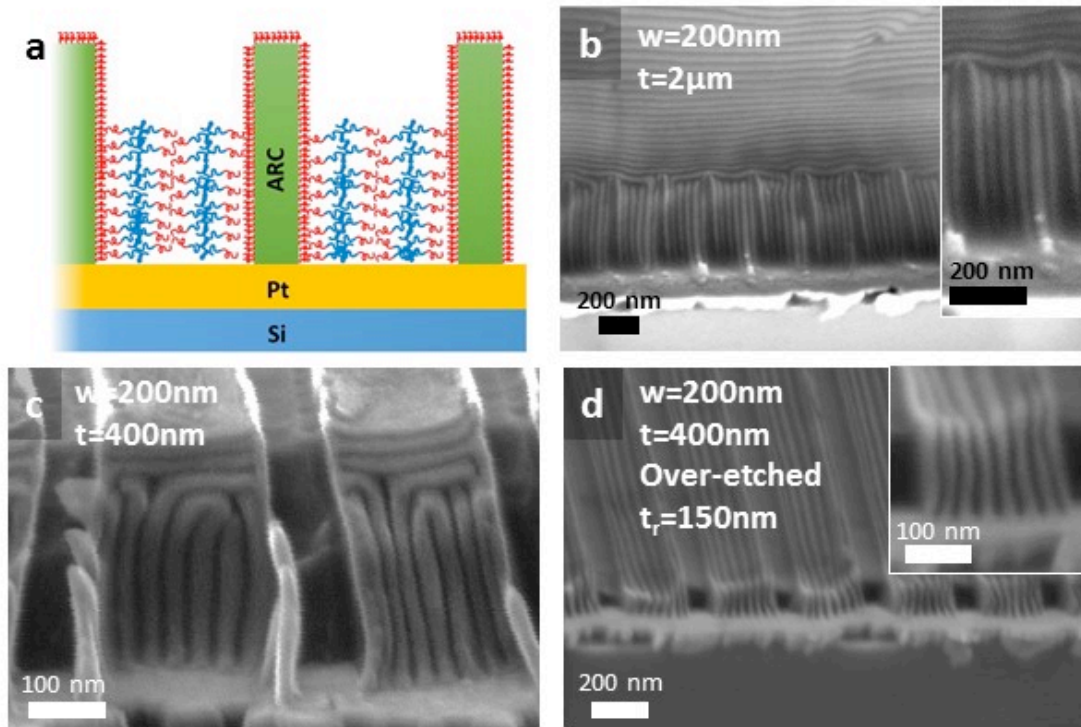
Figure 2. Templates with Pt base, solvent anneal. Lamella-forming block copolymer film in high aspect-ratio gratings with sidewall made of ARC and bottom surface made of Pt. Sidewall surface is attractive to PDMS; Bottom surface is more neutral. (a). Schematic of sample; (b). 85° tilted-view cross-section Helium Ion Microscope (HIM) image of 2μm thick lamella-forming PS-PDMS (SD43) film on the high aspect-ratio gratings after anneal; inset: magnified view; (c). 75° tilted-view cross-section HIM. 400 nm thick SD43 film in high aspect ratio trenches after anneal; (d). 75° tilted-view cross-section SEM. The same 400 nm thick annealed SD43 film was processed by a 30s, 450W CF_4/O_2 plasma etch, planarizing the structure down to $t_r = 150$ nm thickness. (b-d) were annealed under solvent vapor produced from a toluene: heptane 3:1 volumetric mixture for 5hr. w: width of the trench. t: thickness of SD43 film inside trench.
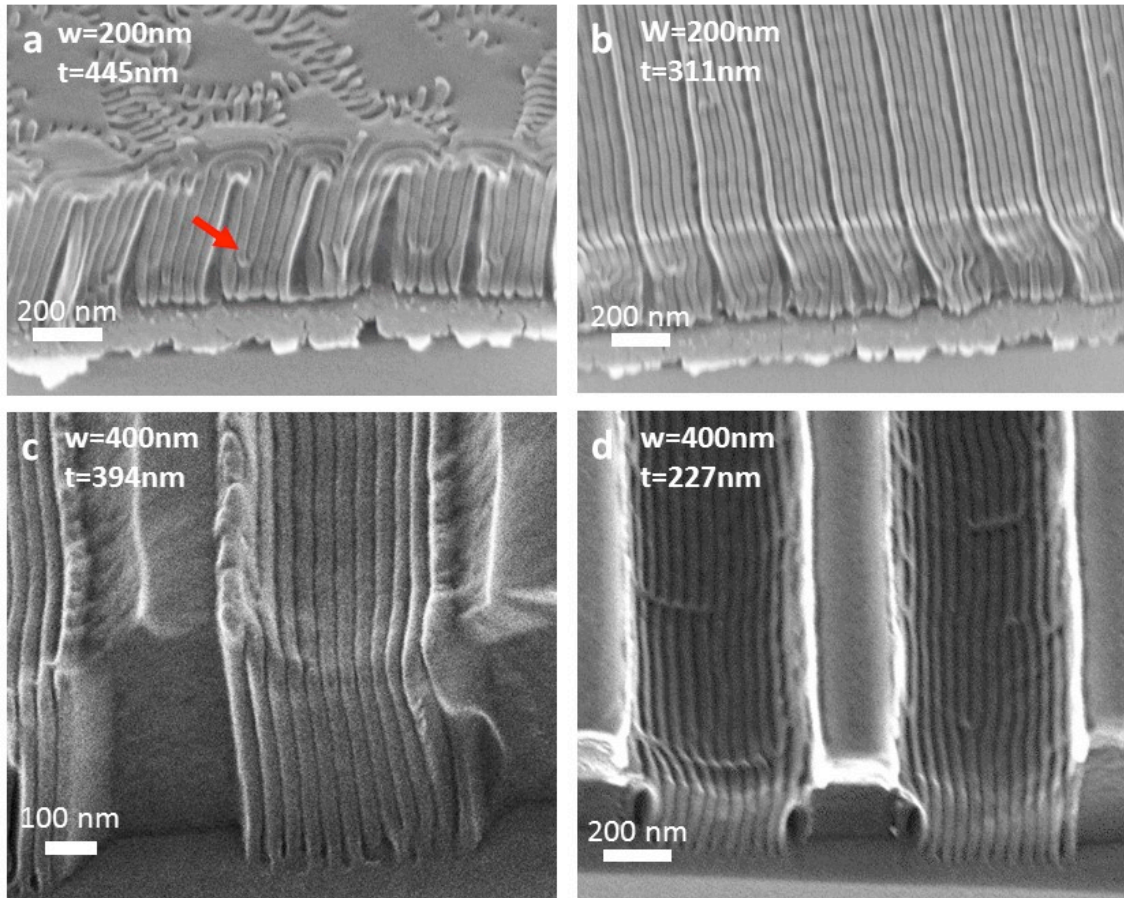
Figure 3. Thermal annealing. 70° tilted helium ion microscope of self-assembled lamella of PS-PDMS. All samples were annealed at 150 °C for 24 hr. a, b, sidewall is ARC, the bottom surface is platinum, ARC grating depth 350 nm, trench width 250 nm; Arrow: one lamella branched into two, a typical defect in perpendicular self-assembled lamellae. c, d. both sidewall and bottom surface are ARC, depth 450 nm, trench width 400 nm; SD43 thickness: a. 445 nm; b. 311 nm; c. 394 nm; d. 227 nm.
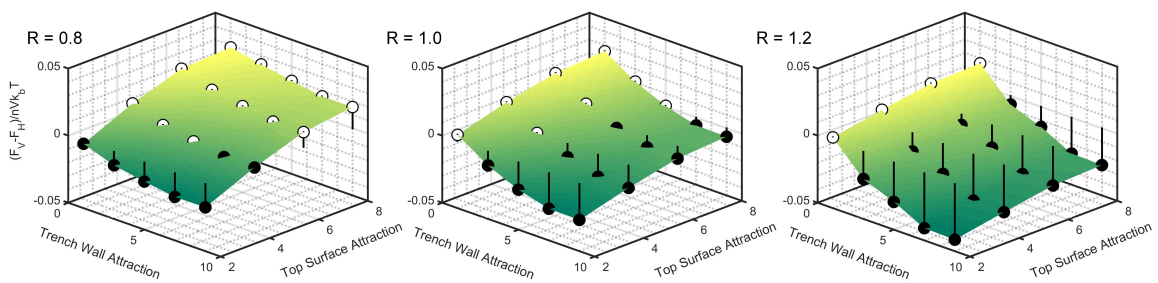
Figure 4. Free energy difference between vertical and horizontal lamellae subjected to trench confinement as a function of top surface attraction field and surrounding trench walls, from SCFT. Free energies are evaluated at surface attractions marked by circular markers. Black filled markers have negative free energy difference indicating stable vertical lamellar structure, while white markers are for stable horizontal lamellae. Aspect ratio R is indicated for every plot.
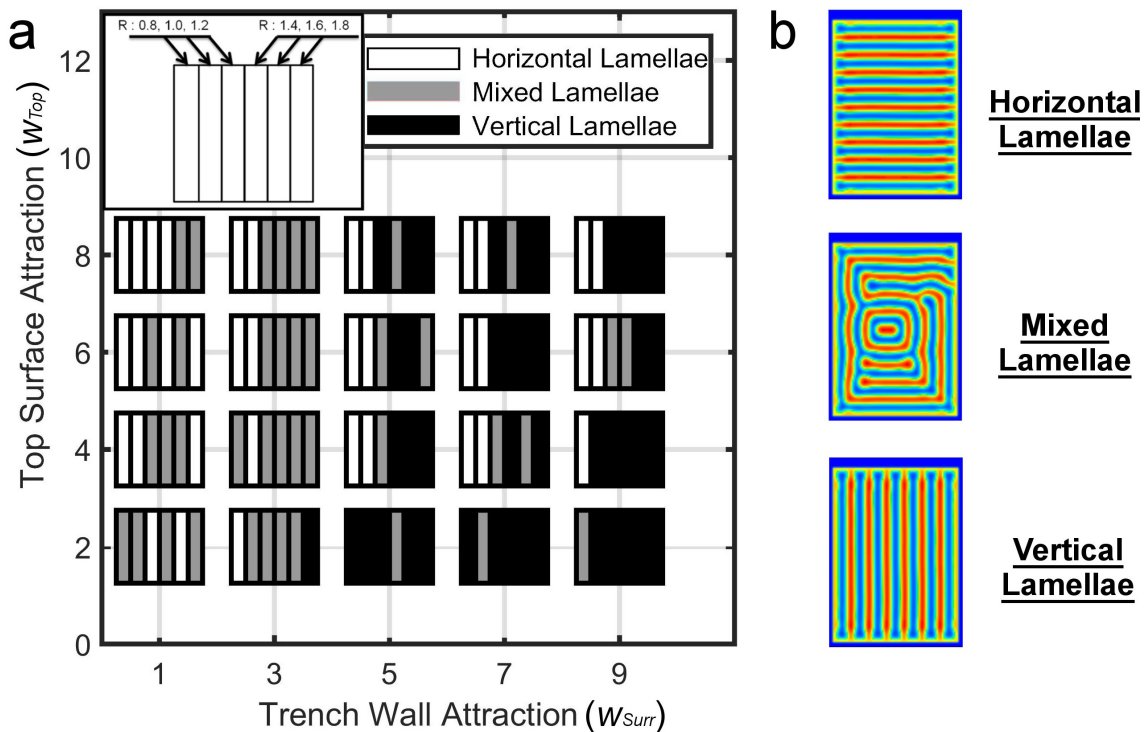

Figure 5. SCFT results. (a) Summary of the equilibrium morphology for simulations evolving from random fields ($\chi N = 14, f = 0.5$). Stripes represent different aspect ratios as explained in the top right corner. The walls are attractive to the red block. At a combination of trench wall and top surface attraction fields, three final structures are obtained: Horizontal lamellae, Mixed lamellae, Vertical lamellae. (b) A representation of the final structures that might emerge from SCFT simulations ($R = 1.4$).
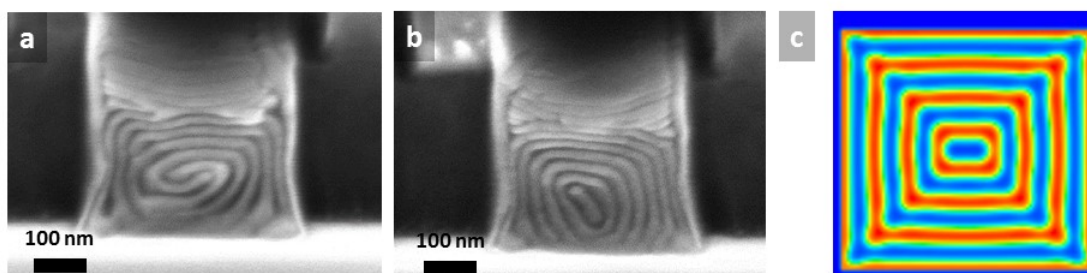

Figure 6. Self-assembled concentric BCP nanotubes. (a), (b) Representative SEM of self-assembled concentric structure. SD43 film with thickness 250 nm in a trench with width 400 nm was processed under solvent vapor from 3 ml toluene: heptane 3:1 volumetric mixture for 24 hr. (c) SCFT results of the density map of polymer A ($R = 1$)

under confinement. A concentric structure is seeded to the simulation and allowed to evolve under varying boundary conditions.
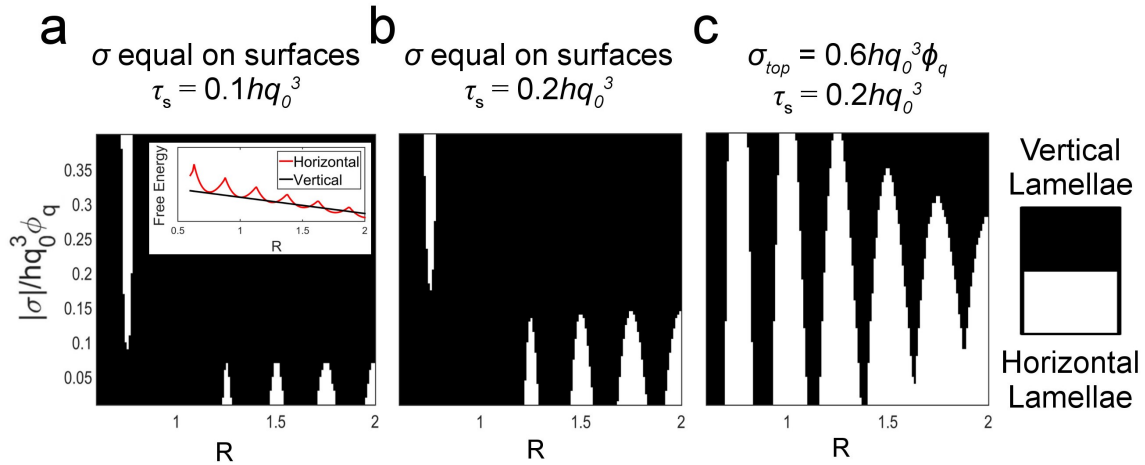

Figure 7. Ginzberg-Landau model. Phase diagram for the stability of vertical (black) and horizontal (white) lamellar structures calculated using GL free energy ($\chi N = 11$). (a) All surfaces are subjected to equal interfacial strength σ and block incompatibility at the surface $\tau_s = 0.1 hq_0^3$ (Inset of free energy of vertical and horizontal lamellae). Vertical lamellae are stable when R and σ are both either high or low. Horizontal lamellae show periodic stable domains due to the strain imposed by the mismatch between the cell height and polymer equilibrium spacing. (b) Increasing $\tau_s = 0.2 hq_0^3$ at the surface extends the stability regions of horizontal lamellae to higher σ. (c) Top surface has a higher affinity σ than the remaining three surfaces causing a significant enhancement of the horizontal lamellae domains even at higher R.